Supplementary Information: Polarization-Resolved Extreme Ultraviolet Second Harmonic Generation from $LiNbO_3$

Can B. Uzundal,[1,2] Sasawat Jamnuch,[3] Emma Berger,[1,2] Clarisse Woodahl,[1,4] Paul Manset,[5] Yasuyuki Hirata,[6] Toshihide Sumi,[7] Angelique Amado,[1,2] Hisazumi Akai,[7] Yuya Kubota,[8,9] Shigeki Owada,[8,9] Kensuke Tono,[8,9] Makina Yabashi,[8,9] John W. Freeland,[10] Craig P. Schwartz,[11] Walter S. Drisdell,[12,13] Iwao Matsuda,[14,7] Tod A. Pascal,[3,15,16,*] Alfred Zong,[1,2] and Michael Zuerch[1,2,17,18,†]

[1] *Department of Chemistry, University of California, Berkeley, California 94720, USA.*
[2] *Materials Sciences Division, Lawrence Berkeley National Laboratory, Berkeley, California 94720, USA.*
[3] *ATLAS Materials Science Laboratory, Department of NanoEngineering and Chemical Engineering, University of California, San Diego, La Jolla, California, 92023, USA.*
[4] *University of Florida, Gainesville, FL 32611, USA.*
[5] *Ecole Normale Superieure de Paris, Paris, France.*
[6] *National Defense Academy of Japan, Yokosuka, Kanagawa 239-8686, Japan.*
[7] *Institute for Solid State Physics, The University of Tokyo, Kashiwa, Chiba 277-8581, Japan.*
[8] *RIKEN SPring-8 Center, Sayo, Hyogo, 679-5148, Japan.*
[9] *Japan Synchrotron Radiation Research Institute, (JASRI), Sayo, Hyogo, 679-5198, Japan.*
[10] *Advanced Photon Source, Argonne National Laboratory, Argonne, IL 60439, USA.*
[11] *Nevada Extreme Conditions Laboratory, University of Nevada, Las Vegas, Las Vegas, NV 89154, USA.*
[12] *Chemical Sciences Division, Lawrence Berkeley National Laboratory, Berkeley, California 94720, USA.*
[13] *Joint Center for Artificial Photosynthesis, Lawrence Berkeley National Laboratory, Berkeley, California 94720, USA.*
[14] *Trans-scale Quantum Science Institute, The University of Tokyo, Bunkyo-ku, Tokyo 113-0033, Japan.*
[15] *Materials Science and Engineering, University of California San Diego, La Jolla, California, 92023, USA.*
[16] *Sustainable Power and Energy Center, University of California San Diego, La Jolla, California, 92023, USA.*
[17] *Fritz Haber Institute of the Max Planck Society, 14195 Berlin, Germany.*
[18] *Friedrich Schiller University Jena, 07743 Jena, Germany.*

CONTENTS

S1: EXTRACTING THE SECOND HARMONIC SUSCEPTIBILITY FROM EXPERIMENTAL DATA

An image from the MCP detector is shown in Fig. S1. Pixels on the reduced detector image are vertically binned to generate a spectrum from every detector image (180,000 to 480,000 spectra per photon energy). A Gaussian function is fit to the fundamental in each shot. If the coefficient of determination (R^2) for the fit is below 0.90, the shot is discarded. Histograms of the shots that satisfy the R^2 criteria was formed with respect to the energy of the fundamental. Among the shots that fall within an energy bin, a histogram with respect to the intensity of the fundamental was formed. At each energy and intensity bin an average of all the shots that fall within the bin is calculated and is represented as a spectrum. An example of one such spectra is shown in Fig. S2a. For each intensity bin at the same energy, a Gaussian is fit to the second harmonic and its area is integrated using the trapezoidal rule. Plotting the second harmonic intensity vs. the fundamental intensity gives a quadratic relationship that can be used to extract the χ^2 as a function of photon energy as shown in Fig. S2b. All data visualizations and array operations were done in Python 3.8 using Matplotlib[1], Numpy[2] and Scipy[3] under a Python(x,y) IDE.

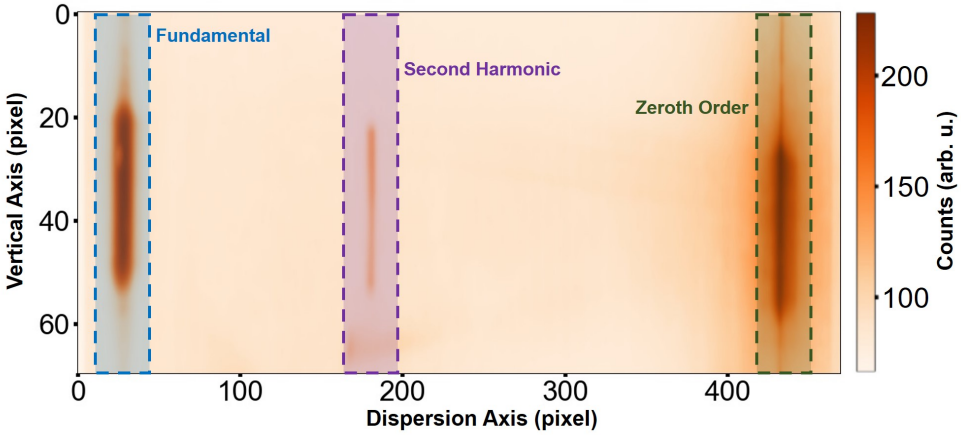

FIG. S1. A representative detector image of the spectrally resolved experiment showing the features of interest, the fundamental, the second harmonic and the zeroth diffraction order.

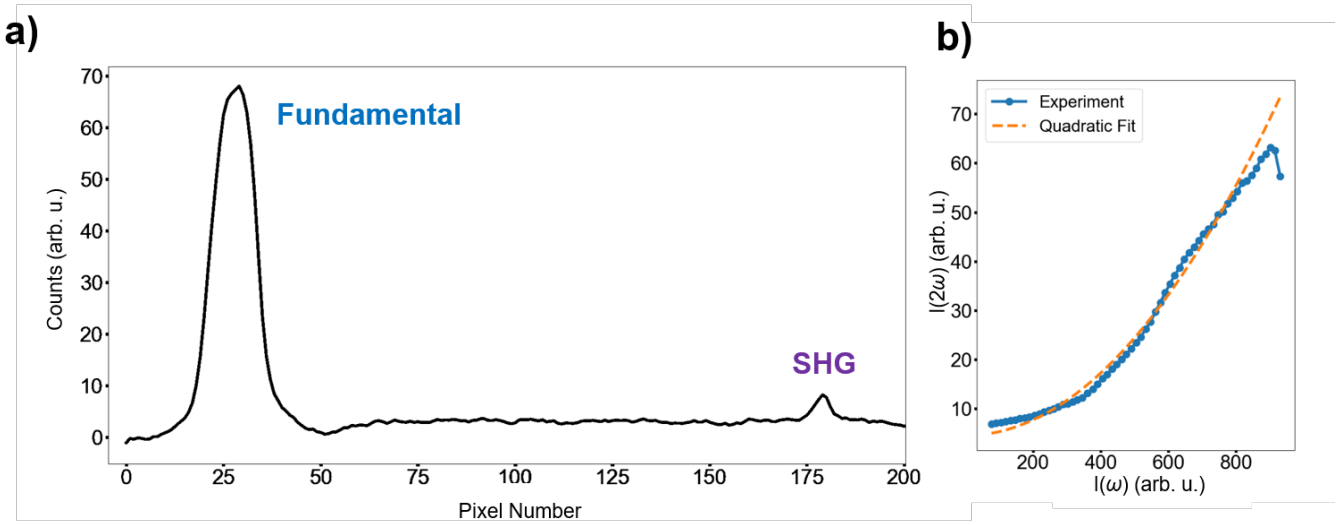

FIG. S2. Overview of the spectral data extracted from the raw detector images. a) Processed spectra, after binning with respect to both energy and intensity at 29 eV. b) Quadratic dependence of the second harmonic intensity to the fundamental at 29 eV.

S2: EXTRACTING THE SECOND HARMONIC POLARIZATION FROM EXPERIMENTAL DATA

The polarization of the emitted light after the sample is measured by a MCP. The MCP measures both the reflected fundamental and the emitted second harmonic while the angular dependence is captured by the rotating multilayer mirror. Shot-to-shot characteristics of the incident beam and the measured output as a function of the polarizer angle is summarized in Fig. S3. The most evident feature in the shot-to-shot characteristics is the presence of two distinct regimes as a function of incident beam intensity (denoted by i_1 in Fig. S3). At lower incident intensities, the measured voltage is linear while at higher incident intensities a quadratic relationship is seen.

At low incident intensities, polar plots show a dipole shape. This is the standard response of polarized linear light which passes through a polarizer (Malus' Law). The linear response is also verified by our experiments at lower incident intensities that are below the threshold to generate the second harmonic as shown in Fig. S4a. The polarization of the second harmonic was isolated from the data by a linear background subtraction at each angle.

The second harmonic signal is more challenging to measure due to its low amplitude so averaging is required to achieve good signal-to-noise ratio. The polarization of both the fundamental and SHG is independent of the incident intensity such that at a given angle, if properly normalized, all of the histograms can be averaged. In Fig. S4a, a data set that contains only the fundamental response which serves as our benchmark is shown. In Fig. S4b, the extracted portion of the fundamental from the total signal for a data set containing both the linear and the second harmonic response is shown. Polarization of the fundamental shows excellent agreement for both cases. The second harmonic portion of the response is treated similarly and the results are shown in Fig. 4 of the main text.

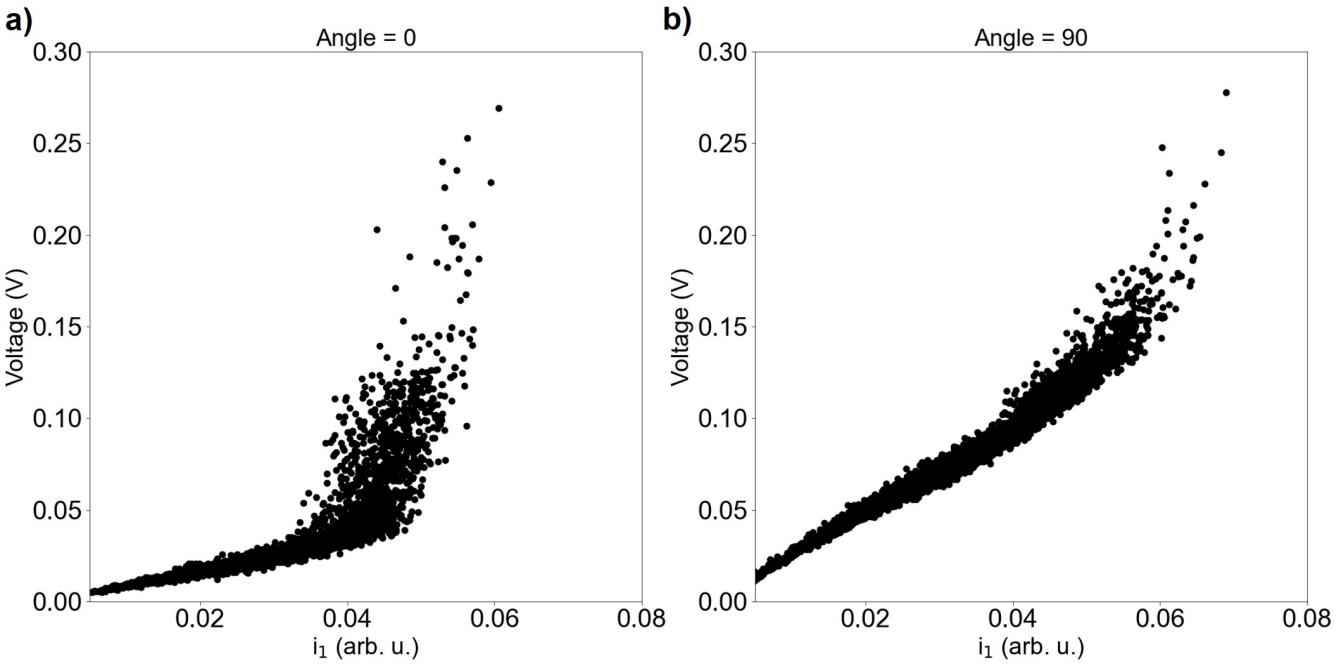

FIG. S3. Shot-to-shot characteristics of the polarimetry data at 33 eV as a function of incident beam intensity. The nonlinear portions shown describe the contribution from the second harmonic signal to the measured voltage and is clearly dependent on the polarizer angle [(a) detector angle $\phi = 0^\circ$ and b) detector angle $\phi = 90^\circ$.].

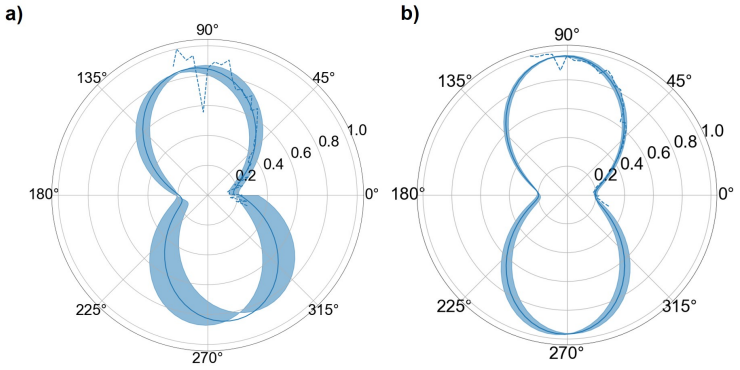

FIG. S4. The reproducibility of the extracted data can be verified by comparing the polarization of the fundamental for different data sets. a) The polarization of the fundamental for a data set without the second harmonic response (The linearity of the response was ensured by attenuating the incident fundamental intensity). b) The polarization of the fundamental extracted from a data set containing the second harmonic response.

S3: DETERMINING THE EFFECTIVE SECOND HARMONIC SUSCEPTIBILITY

The second order polarization of the medium can be described by a generalization of the linear optical response[4].

$$P_i(2w) = \varepsilon_0 \chi^{(2)}_{ijk} E_j(w) E_k(w) \tag{1}$$

Looking at the expression for the polarization, the figure that ties the incident fundamental's orientation in space to the polarization in the crystal lattice is the tensor, $\chi^{(2)}_{ijk}$. As the tensor is sensitive to crystal symmetry, depending on the facets of the crystal the beam is incident on, the nonlinear susceptibility tensor needs to be rotated to match the cut of the crystal investigated. Inspecting the crystal structures shown in Fig. S5, for the z-cut $LiNbO_3$, the optical axis aligns with the principal symmetry axis and the tensor for C_{3v} symmetry could be used as is. For the x-cut $LiNbO_3$, however, the optical axis and the principal symmetry axis does not align. In Fig. S6 the relative orientation

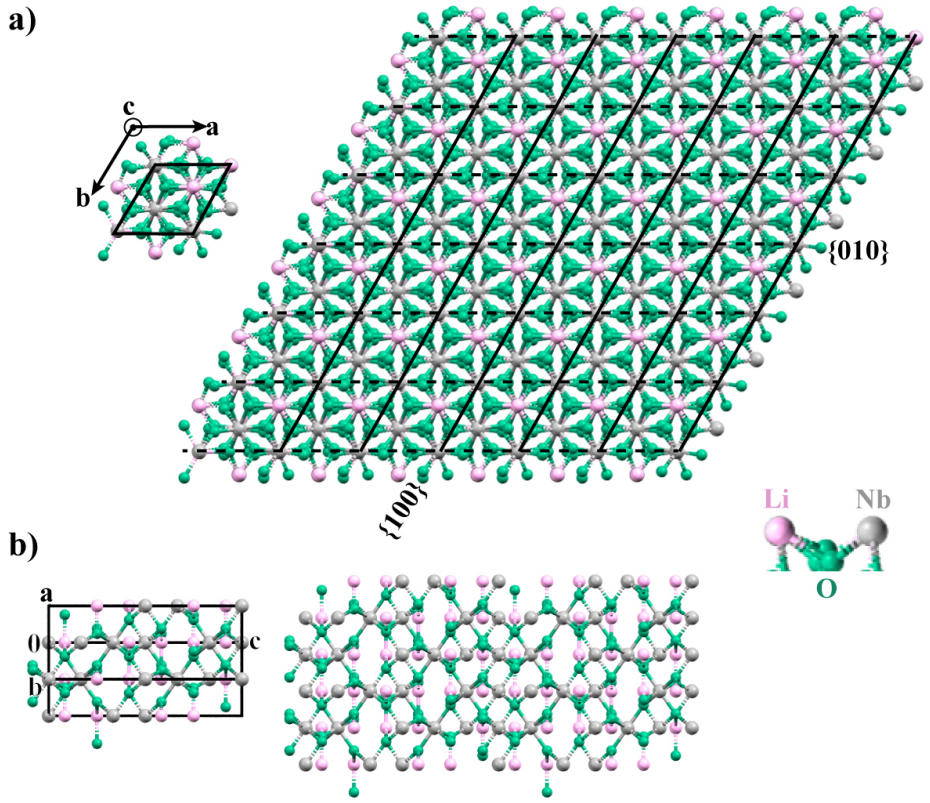

FIG. S5. The orientation of the $LiNbO_3$ crystal is critical for the polarization response. a) The orthorhombic crystal when viewed looking down on the lattice vector c is shown. Crystal plane families {100} and {010} are also shown in full and dashed lines respectively to highlight the unit cell. The optical axis of the z-cut is along the lattice vector c. Note the threefold symmetry of the [001] plane. b) The crystal structure when viewed perpendicular to the [100] plane, which corresponds to the optical axis of the x-cut.

of the cartesian coordinates, lattice vectors (a, b, c) and the principal symmetry axis, C_3 along with the orthorhombic lattice is shown along with the rotations that needs to be performed. The tensor for the z-cut crystal is the following:

$$\chi^{(2)}_{ijk} = \begin{bmatrix} 0 & d_{xyx} & d_{yzy} \\ d_{xyx} & 0 & 0 \\ d_{yzy} & 0 & 0 \\ \\ d_{xyx} & 0 & 0 \\ 0 & -d_{xyx} & d_{yzy} \\ 0 & d_{yzy} & 0 \\ \\ d_{zyy} & 0 & 0 \\ 0 & d_{zyy} & 0 \\ 0 & 0 & d_{zzz} \end{bmatrix}$$

while the tensor for the x-cut crystal is

$$\chi^{(2)}_{ijk} = \begin{bmatrix} d_{zzz} & 0 & 0 \\ 0 & d_{zyy} & 0 \\ 0 & 0 & d_{zyy} \\ \\ 0 & d_{yzy} & 0 \\ d_{yzy} & d_{xyx} & 0 \\ 0 & 0 & -d_{xyx} \\ \\ 0 & 0 & d_{yzy} \\ 0 & 0 & -d_{xyx} \\ d_{yzy} & -d_{xyx} & 0 \end{bmatrix}$$

Using these tensors, the angular anisotropy of SHG is calculated for all possible combinations of incident fundamental and emitted harmonic polarizations are shown in Fig. S8. These calculations were performed using the `ShgPy` package[5,6].

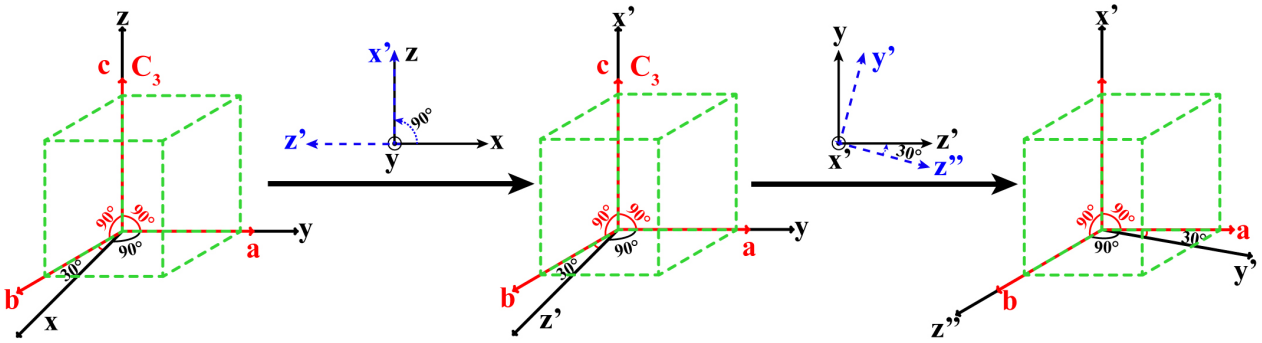

FIG. S6. The orthorhombic unit cell vectors (a, b, c) and the coordinate system of the unrotated tensor (x, y, z) for the z-cut $LiNbO_3$ is shown. The two rotations that need to be performed to align the z-axis (the optical axis) with the lattice vector b (the unit vector along {010} plane family) is shown.

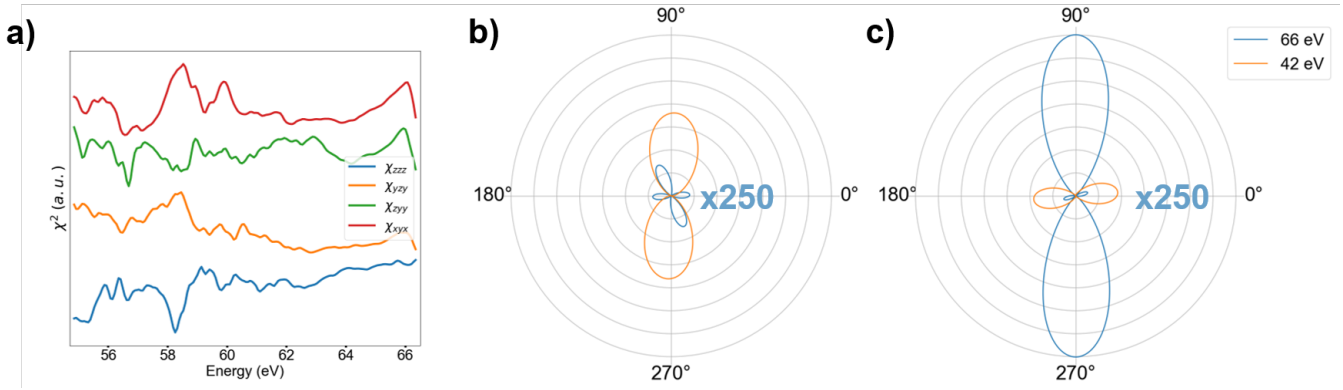

FIG. S7. Overview of the numerical results. (a) Calculated values of the individual tensor elements of the the $\chi^{(2)}$ tensor for $LiNbO_3$ as a function of the SHG energy. (b),(c) Predicted rotational anisotropy response of SHG at two energies 42 and 66 eV as a function of crystal rotation for p-polarized incident light and p polarized SHG (b), p-polarized incident light and s polarized SHG (c).

For completeness, the expression for the angular anisotropy calculation for the x-cut in the p in s out channel is:

$$\begin{aligned} I^{ps}(2w) \propto (&0.5d_{xyx}\sin^2(\gamma)\cos(\gamma) - 0.5d_{xyx}\cos(\gamma) - d_{yzy}\sin(\gamma)\cos^2(\gamma) \\ &+0.5d_{zyy}\sin^3(\gamma) + 0.5d_{zyy}\sin(\gamma) + 0.5d_{zzz}\sin(\gamma)\cos^2(\gamma))^2 \end{aligned} \tag{2}$$

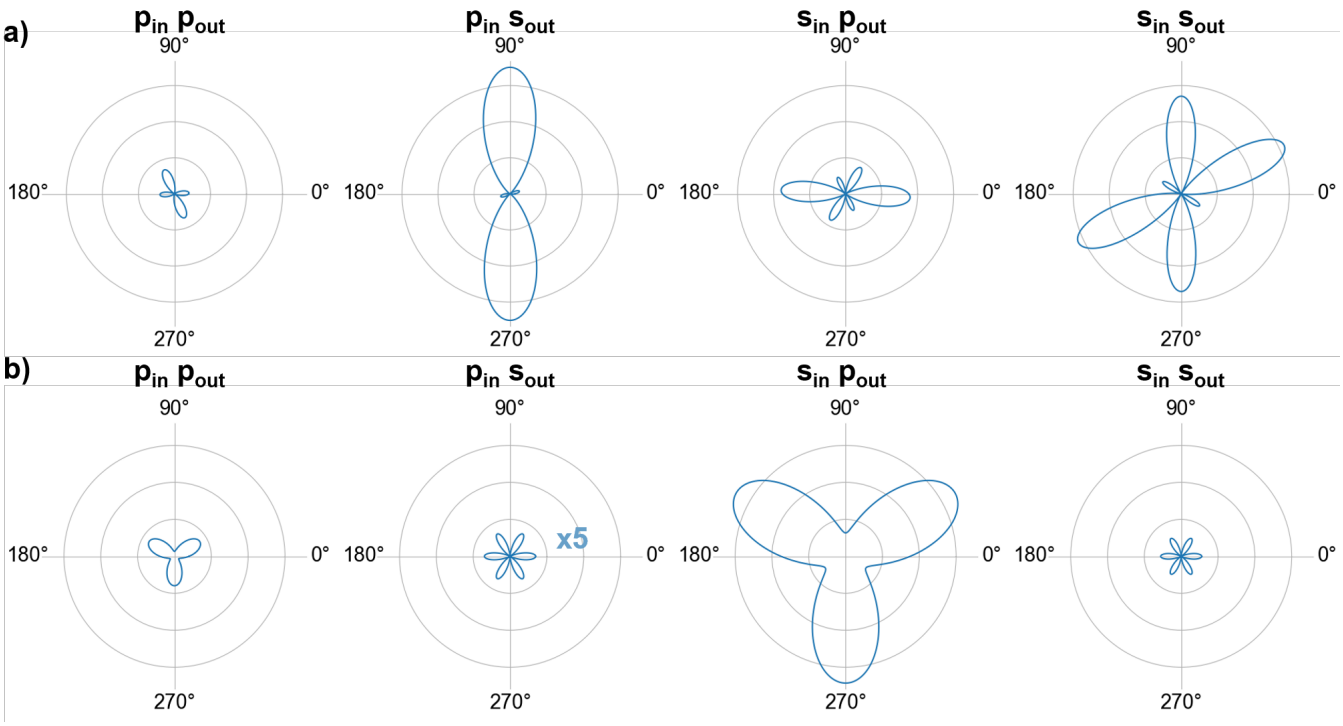

FIG. S8. Calculated SHG polarimetry response of $LiNbO_3$ at 66 eV using the numerical values of the individual tensor elements. All 4 combinations of the possible incidence and detection polarizations are shown for a) x-cut $LiNbO_3$ b) z-cut $LiNbO_3$

x-cut in the p in p out channel is:

$$I^{pp}(2w) \propto 0.25(-0.5d_{xyx}\sin^3(\gamma) - 0.5d_{xyx}\sin(\gamma) + d_{yzy}\sin^2(\gamma)\cos(\gamma) - d_{yzy}\cos(\gamma) \\ +0.5d_{yzy}\sin^2(\gamma)\cos(\phi) + 0.5d_{zyy}\cos(\gamma) + 0.5d_{zzz}\cos^3(\gamma))^2 \quad (3)$$

The $\chi^2_{eff}(w)$ described in the main text is calculated as a sum of these two polarization components shown in Eq.2 & 3 with $\gamma = 90°$.

The patterns shown in Fig. S7(b) & (c) and Fig. S8(a) are the **intensity** of the emitted second harmonic as a function of in-plane rotation (denoted as γ) of the x-cut $LiNbO_3$, where the panels show the angular anisotropy patterns for the two polarization channels (p and s). The comparison between the calculations [Fig. S7(b) & (c) and Fig. S8(a)] and the polarization experiment (Fig. 3) should not be made on the basis of the shape of these plots. Comparing the calculated intensity of SHG at 66 eV between the p in p out [Fig S7(b), blue line] and p in s out channels [Fig S7(c), blue line], one can see that the majority of the emitted intensity is s-polarized. This majority s-polarization was resolved using the *polarizer* described in the main text.

S4: DETERMINATION OF OPTICAL COMPONENTS N AND K OF LINBO$_3$

The refractive index of $LiNbO_3$ over an energy range of $\sim$ 25–75 eV was determined by measuring the reflected signal at a variety of angles at the Advanced Light Source at the Lawrence Berkeley National Laboratory (Beamline 6.3.2). This was then used to invert Fresnel's equation to extract the real and imaginary part of the refractive index using a procedure by Kaplan et al.[7].

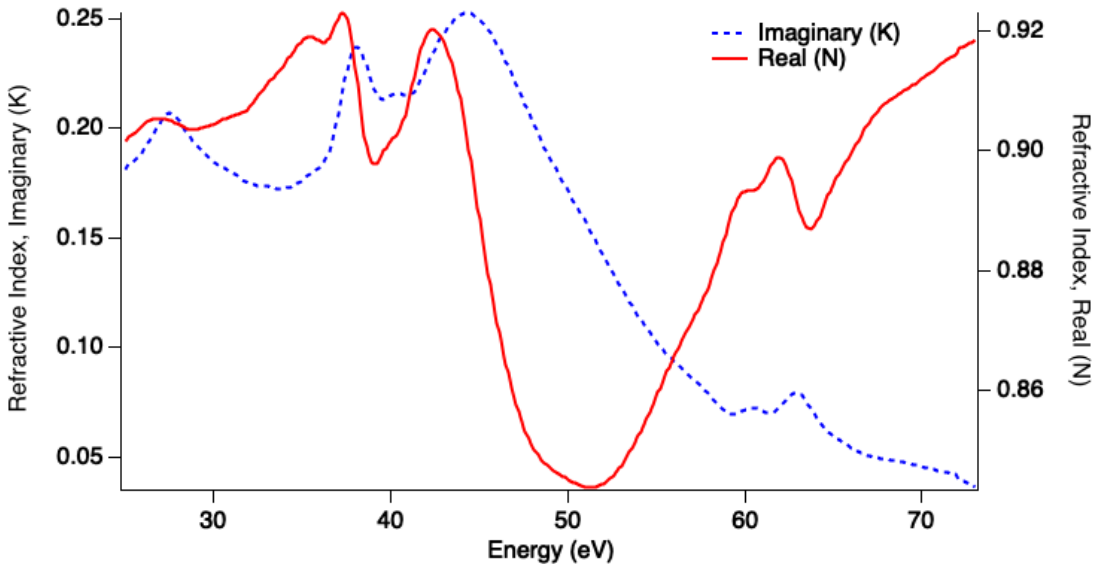

FIG. S9. Measured values the imaginary (K, blue, dotted) and real (N, red, solid) components of the refractive index of $LiNbO_3$.

S5: THEORETICAL METHODS

S5.1: Calculation of core and valence effects

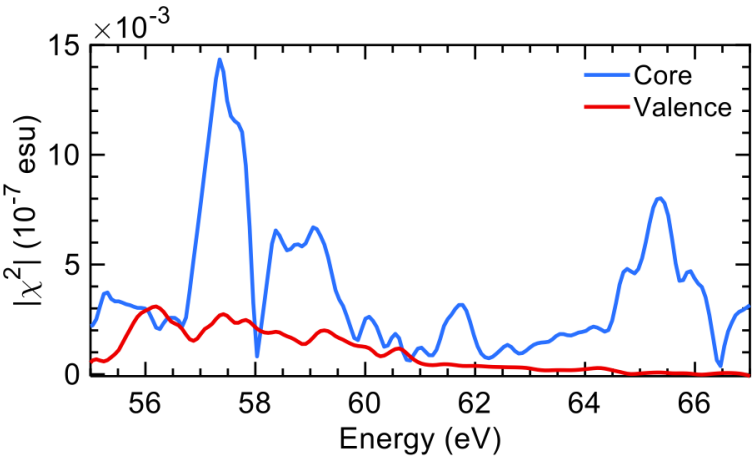

FIG. S10. Calculated spectrum of $LiNbO_3$ due to core (blue) and valence (red) electrons.

To verify that the resonant contribution for $LiNbO_3$ is mainly from the core electrons, we developed an improved calculation scheme that allows us to select specific bands from DFT calculation for second order nonlinear susceptibility calculation. We showed that the core resonant contribution is the main response at XUV regime and accounts for at least 70% of the total signal. In Fig. S10, we observed that the bulk of the signal is due to the resonant excitation of core electrons as compared to valence electrons. Note that the calculation of $\chi^{(2)}_{\text{eff}}(w)$ is in absolute units.

S5.2: Calculation of symmetry effects

To determine the effect of symmetry breaking on the SHG signal, the signal was calculated in both a centrosymmetric and non-centrosymmetric structure of $LiNbO_3$. The breaking of symmetry increases the signal by roughly seven orders of magnitude, as demonstrated in Fig. S11. Note that the calculation of $\chi^{(2)}_{\text{eff}}(w)$ is in absolute units.

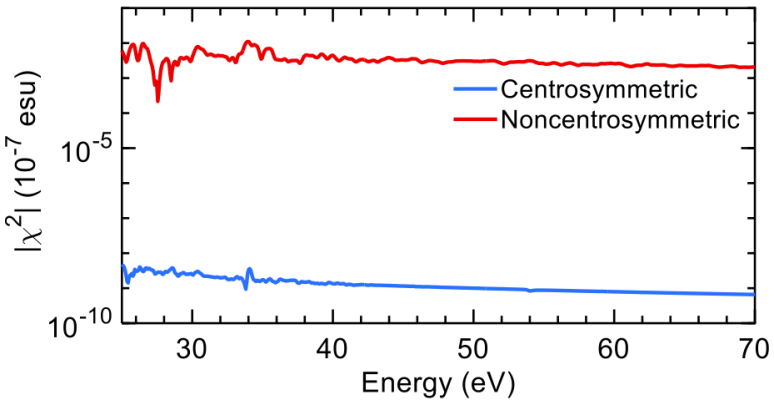

FIG. S11. Calculated spectrum of $LiNbO_3$ in a centrosymmetric (blue) and non-centrosymmetric (red) structure.

S5.3: Determination of element specific effects

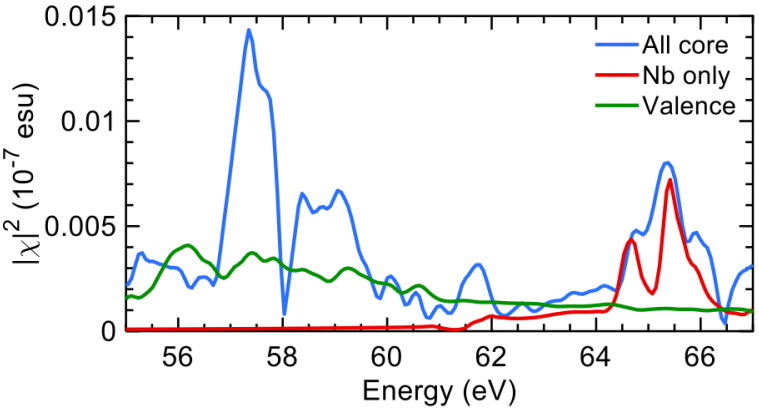

FIG. S12. Calculated spectrum of $LiNbO_3$ decomposed into its elemental components.

Here, we show the effect of specific element contributions. The effect of both elements is not an 'on' and 'off' as a function of energy, but rather one energy becomes increasingly dominant as seen in XAS[8]. The calculations matches the assignment based on the well established edge energies of the relevant transitions[9]. In Fig. S12, we calculate the second order susceptibility and decompose it into elemental contribution. The Nb semicore electron contribution (red) is isolated to show that it has no significant contribution to the first two peaks. Here, we verify that the first two major peaks are only then possible due to Li 1s transition (primarily blue). While the peaks around 65 eV are due to Nb semicore electron transition. The valence background, which is roughly a constant background, is shown in green.

S5.4: Single point calculations of Li ion displacement along the polar axis

To demonstrate the ferroelectric property of $LiNbO_3$ due to Li ion displacement along the polar axis. The simulation is performed using Vienna Ab initio Simulation Package (VASP). A rhombohedral unit cell of $LiNbO_3$ with cell length of 5.54373 and angle of 55.7562° was sampled using gamma point centered k-grid of 12×12×12. We employed PAW pseudopotential with PBE exchange correlation functional. In Fig. S13, we observed the quantum double well feature

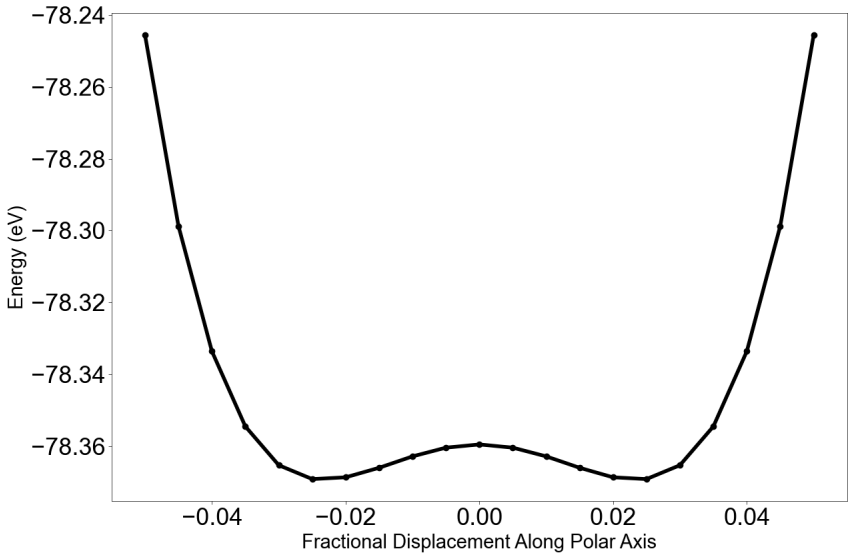

FIG. S13. Energy of $LiNbO_3$ as a function of Li fractional displacement along polar axis

showing favorable energy of the system if the Li atoms were displaced from the centrosymmetric position. Due to the displacement of Li atoms, the ferroelectric property of $LiNbO_3$ is present, however should the temperature rise beyond 1145 °C, the material would lose its ferroelectricity.

S5.5: Molecular dynamics simulation of $LiNbO_3$

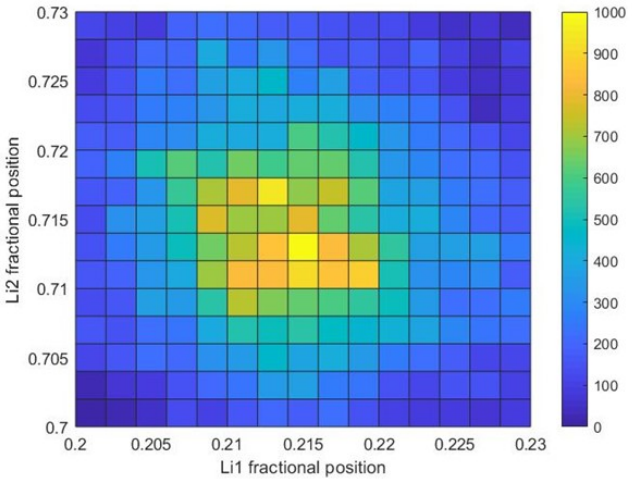

FIG. S14. Bivariate histogram of Li atoms fractional position along the polar axis.

While single point calculation based on the structure can give useful information, the finite temperature motion gives rise to the fluctuation in the system of interest. Due to this phenomena, the thermodynamics properties of any given material should be averaged from all thermodynamically possible structures. Hence, to provide accurate result for linear and nonlinear response, the molecular dynamics (MD) simulation of $LiNbO_3$ is performed in VASP to obtain different snapshot of the system. The centrosymmetric $LiNbO_3$ unit cell was propagated with 0.5 fs timestep using Nose-Hoover thermostat and 4×4×4 Γ-point centered k-point grid. The temperature is set to 300 K the same as the experimental value. The equilibrated trajectory were then collected for different snapshots of the structure then Boltzmann averaged to find their respective contributions. The Li fractional positions along the polar axis is sorted into a histogram. We observed that Li atoms displaced from the centro-symmetric position. The population favors approximately 0.35 fractional unit displacement which translates to 0.487Å which is slightly higher than from the single point calculation. The difference between molecular dynamics and single point calculation is due to the removal of restriction on the movement of both oxygen and niobium which allows more favorable structures. Lastly, while this finite temperature motion may not have significant effect on linear response, nonlinear response is more susceptible to the change which can be crucial for accuracy. As the nonlinear response is more susceptible to the subtle changes in the unit cell, the origin of the measured $\chi^{(2)}_{\text{eff}}(w)$ (labeled as transition # 3 in the main text) involving Nb states was further investigated with molecular dynamics simulations. Two key types of distortions that break the inversion symmetry and contribute to the $\chi^{(2)}_{\text{eff}}(w)$ can be analyzed. Namely these distortions are the distortions to the Nb-O bond length and variations in the Nb-O-polar axis angle as a result of the ferroelectric displacement. Due to lithium displacement, the Nb-O bond on one side of the unit cell is elongated while on the other side it is contracted [Fig. S15(a)]. The elongated bonds also have a broadened distribution as they have more space to explore in the unit cell [Fig. S15(b)]. Consequently, this results in two distinct angle distributions for Nb-O on the two sides of the unit cell. Nb ion on the other hand is relatively static and does not get substantially displaced. The overall orientation of NbO_6 octahedral cage with respect to the original non-polar phase shows minimal change in the tilting of the octahedra [Fig. S15(b) & (c)]. All in all, the tilting of octahedron cage in either phase is relatively small and is within a few degrees. In conclusion, the NbO_6 octahedral cage, like Nb ion, is relatively static in $LiNbO_3$.

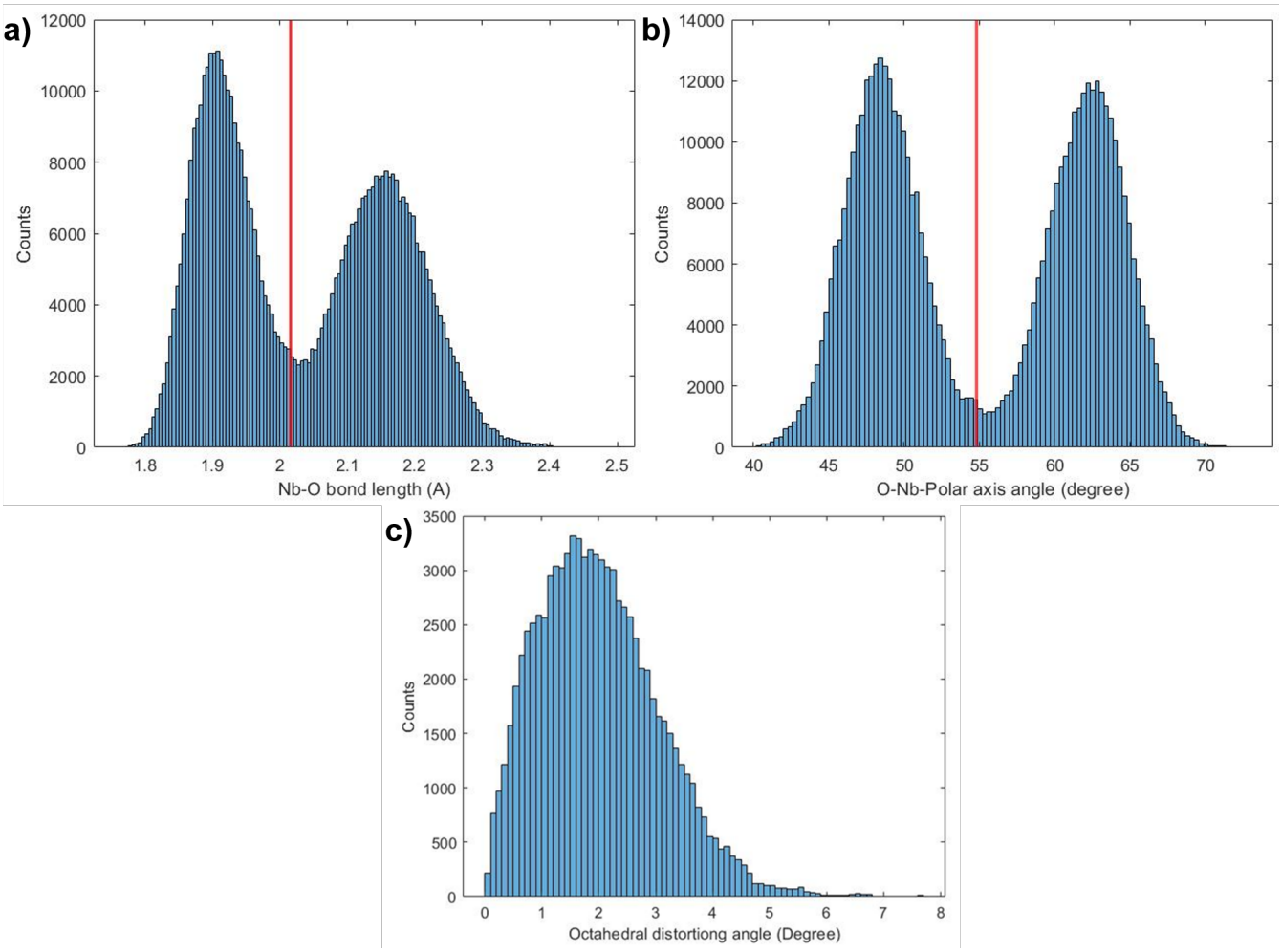

FIG. S15. Histograms of the molecular dynamics simulations of $LiNbO_3$ focusing on the Nb ion environment. The distribution of (a) Nb-O bond lengths, (b) O-Nb-polar axis angle, is shown as a histogram for the ferroelectric phase. The red-line is the value of the bond length for the paraelectric phase. (c) The distribution of the octahedral distortion angles for the paraelectric phase.

S6: MEASUREMENTS OF THE LINEAR RESPONSE OF $LINBO_3$

The absolute reflectivity of $LiNbO_3$ was measured at beamline 6.3.2 of the Advanced Light Source at the Lawrence Berkeley National Laboratory[10]. Using a previously described numerical algorithm the real and imaginary parts of the dielectric function was extracted from the measured absolute reflectivity[7]. The imaginary part of the linear response was used to verify our theoretical calculations is shown in Fig. S16.

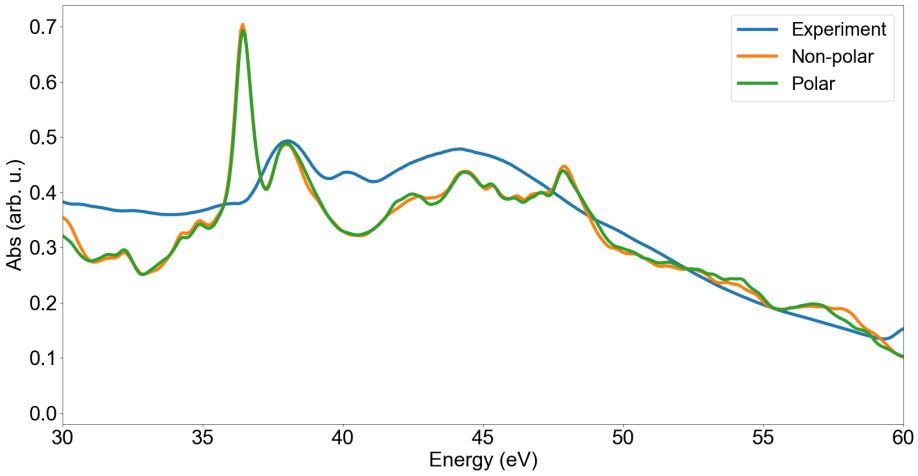

FIG. S16. Imaginary part of the dielectric functions for centrosymmetric and non-centrosymmetric $LiNbO_3$ in comparison to measured XAS.

---

* Correspondence to: tpascal@ucsd.edu
† Correspondence to: mwz@berkeley.edu

[1] J. D. Hunter, "Matplotlib: A 2d graphics environment," Comput. Sci. Eng. **9**, 90–95 (2007).
[2] C. R. Harris, K. J. Millman, S. J. van der Walt, R. Gommers, P. Virtanen, D. Cournapeau, E. Wieser, J. Taylor, S. Berg, N. J. Smith, et al., "Array programming with NumPy," Nature **585**, 357–362 (2020).
[3] P. Virtanen, R. Gommers, T. E. Oliphant, M. Haberland, T. Reddy, D. Cournapeau, E. Burovski, P. Peterson, W. Weckesser, J. Bright, et al., "SciPy 1.0: Fundamental Algorithms for Scientific Computing in Python," Nat. Methods **17**, 261–272 (2020).
[4] R. W. Boyd, Nonlinear Optics, 3rd ed. (Academic Press, 2008).
[5] B. T. Fichera, A. Kogar, L. Ye, B. Gökce, A. Zong, J. G. Checkelsky, and N. Gedik, "Second harmonic generation as a probe of broken mirror symmetry," Phys. Rev. B **101**, 241106 (2020).
[6] B. Fichera, "ShgPy," `https://bfichera.github.io/shgpy/` (2020).
[7] C. J. Kaplan, P. M. Kraus, E. M. Gullikson, L. J. Borja, S. K. Cushing, M. Zürch, Hu. Chang, D. M. Neumark, and S. R. Leone, "Retrieval of the complex-valued refractive index of germanium near the m4,5 absorption edge," J. Opt. Soc. Am. B **36**, 1716–1720 (2019).
[8] Laurent D. Menard, Qi Wang, Joo H. Kang, Andrew J. Sealey, Gregory S. Girolami, Xiaowei Teng, Anatoly I. Frenkel, and Ralph G. Nuzzo, "Structural characterization of bimetallic nanomaterials with overlapping x-ray absorption edges," Phys. Rev. B **80**, 064111 (2009).
[9] John C. Fuggle and Nils Mårtensson, "Core-level binding energies in metals," Journal of Electron Spectroscopy and Related Phenomena **21**, 275–281 (1980).
[10] J. H. Underwood, E. M. Gullikson, M. Koike, P. J. Batson, P. E. Denham, K. D. Franck, R. E. Tackaberry, and W. F. Steele, en"Calibration and standards beamline 6.3.2 at the Advanced Light Source," Review of Scientific Instruments **67**, 3372–3372 (1996).